Journal of
Marine Science and Engineering

MDPI

Article

Near-Bottom Magnetic Anomaly Features and Detachment Fault Morphology in Tianxiu Vent Field, Carlsberg Ridge, Northwest Indian Ocean

Shuang Du [1,2], Zhaocai Wu [2,*], Xiqiu Han [1,2,3,*], Yejian Wang [1,2], Honglin Li [2] and Jialing Zhang [2,3]

1 Institute of Sedimentary Geology, Chengdu University of Technology, Chengdu 610059, China
2 Key Laboratory of Submarine Geosciences & Second Institute of Oceanography, Ministry of Natural Resources, Hangzhou 310012, China
3 Ocean College, Zhejiang University, Zhoushan 316021, China
* Correspondence: wuzc@sio.org.cn (Z.W.); xqhan@sio.org.cn (X.H.)

Abstract: As a product of hydrothermal mineralization at spreading centers, seafloor massive sulfides (SMS) have become a research hotspot in the field of prospecting and exploring deep-sea mineral resources owing to their enrichment of various strategic metals. Since hydrothermal circulation changes the magnetic properties of host rocks and can generate magnetic anomalies, near-bottom magnetic surveying is an effective method to determine magnetic anomaly features of the seafloor. This technology has been applied to the detection of SMS deposits, in addition to its use in understanding hydrothermal fluid flow conduits and associated hydrothermal alterations. The Tianxiu Vent Field (TVF) is a detachment-fault-controlled, ultramafic-associated hydrothermal system located on the Carlsberg Ridge, Northwest Indian Ocean. During China's DY57th cruise in 2019, near-bottom magnetic data were collected by an autonomous underwater vehicle. In this paper, we use bathymetric and magnetic data, as well as rock sampling information, to analyze and discuss the magnetic anomaly features of the TVF region. Then, we apply 2.5D magnetic anomaly profile forward modeling to determine the shallow magnetic structure and the pattern of detachment faults in the subsurface. Our results show that TVF is characterized by a significant positive magnetic anomaly, where stronger magnetization exists in the area with active hydrothermal vent clusters. The detachment fault has a dip of less than 30° at shallow depths, which steepens to a dip of ~70° at depths of around 300 m.

Keywords: Tianxiu Vent Field; ultramafic-associated hydrothermal systems; near-bottom magnetic anomaly; detachment fault

Citation: Du, S.; Wu, Z.; Han, X.; Wang, Y.; Li, H.; Zhang, J. Near-Bottom Magnetic Anomaly Features and Detachment Fault Morphology in Tianxiu Vent Field, Carlsberg Ridge, Northwest Indian Ocean. *J. Mar. Sci. Eng.* **2023**, *11*, 918. https://doi.org/10.3390/jmse11050918

Academic Editor: Assimina Antonarakou

Received: 4 March 2023
Revised: 7 April 2023
Accepted: 13 April 2023
Published: 25 April 2023

1. Introduction

Since the first observation of seafloor hydrothermal activity at the East Pacific Rise in 1977 [1], modern seafloor hydrothermal activity and the accompanying seafloor massive sulfides (SMS) have attracted widespread attention from the scientific community [2]. At present, the main techniques for SMS exploration include plume and water anomaly detection, geological sampling, and geophysical exploration. Among these, geophysical methods are important for understanding the spatial distribution of sulfide deposits and hydrothermal circulation processes [3]. Magnetic surveys of seafloor hydrothermal fields have revealed that the hydrothermal alteration of rocks has led to magnetic changes under the influence of hydrothermal fluids [4]. The hydrothermal areas of different bedrock types exhibit different magnetic anomaly characteristics. For basalt-hosted hydrothermal systems, oceanic crust rocks—such as basalt, diabase, and gabbro—present reduced or weakly magnetic anomalies owing to hydrothermal alteration or thermal demagnetization [5–7]. Ultramafic-hosted hydrothermal systems present strong positive magnetic anomalies due to the abundant magnetite produced by the serpentinization of peridotite [8,9]. In addition, the high hydrogen content of high-temperature hydrothermal fluids maintains a strongly reducing environment, which protects magnetite from oxidation [10]. Therefore, the acquisition of near-bottom magnetic fields when exploring and evaluating seafloor sulfide resources is becoming increasingly prominent [11]. In addition, the investigation of magnetic anomalies is not only conducive to examining the different types of seafloor hydrothermal systems [12–14], but also reflects the geometry and distribution of this subsurface crustal structure of active hydrothermal vent systems. As a result, a new research perspective is emerging for systematically exploring the hydrothermal circulation mechanism [15,16]. For example, Tivey et al. [17] analyzed the high-resolution near-bottom magnetic profiles obtained through a near-bottom draped survey over the active Trans-Atlantic Geotraverse (TAG) mound. They found a very-short-wavelength (<100 m) magnetic low directly over the active mound, which was interpreted as a subsurface alteration pipe beneath the active mound or a thermally demagnetized upflow zone. Szitkar et al. [18] reported that both the Rainbow and Ashadze hydrothermal areas on the mid-Atlantic ridge exhibited strong magnetization. This observation reflects the presence of a wide mineralized zone beneath these sites, the stockwork, where several chemical processes concur to create and preserve strongly magnetized magnetite. Tontini et al. [19] applied 3D focused inversion for the near-bottom magnetic data of the hydrothermal system of Brothers Volcano in New Zealand, South Pacific Ocean. This result showed, in particular, how the subsurface 3D magnetization distribution correlates with different vents' field characteristics at focused and diffuse sites. Galley et al. [16] applied minimum-structure inverse modeling to the near-bottom magnetic data collected in Solwara I of the East Manus Basin in the coastal area of Papua New Guinea, imaging the entire structure of a high-temperature convection column, also identifying the top of the underlying magma chamber. However, although some progress has been made, due to the associated technical difficulties and high cost, the application of near-bottom magnetic anomaly surveying at mid-ocean ridges has still been very limited to date.

The Tianxiu Vent Field (TVF) is a detachment-fault-controlled ultramafic-associated hydrothermal system located on Carlsberg Ridge [20]. However, the morphology of the detachment fault and spatial distribution features of the hydrothermal system are still unclear. In 2019, during the China DY57th cruise, we collected near-bottom magnetic and bathymetric data in the Tianxiu Vent Field and its surrounding region by using the "Qianlong III" Autonomous Underwater Vehicle (AUV). In this paper, we analyze the features and sources of near-bottom magnetic anomalies in the Tianxiu Vent Field using near-bottom magnetic and bathymetric data, seafloor observation, and geological sampling. Moreover, the 2.5 dimensional (2.5D) forward modeling of magnetic anomaly profiles [21,22] is used, with the aim of revealing the shallow magnetic structure of the TVF and the geometry of subsurface detachment faults. Our work provides a valuable basis for the establishment of geological models for the seafloor polymetallic sulfide deposits distributed in the TVF and its surrounding regions.

2. Geological Background

The slow-spreading Carlsberg Ridge is located in the Northwest Indian Ocean within 2° S–10° N, with a total length of about 1500 km and a full spreading rate of 22–32 mm/a [23,24]. The Tianxiu Vent Field (63°50′ E, 3°41′ N) is a typical off-axis vent system, and lies on the south slope of the asymmetric expansion segment of Carlsberg Ridge, with an off-axis of about 5 km at a water depth of 3000–3600 m (Figure 1a,b). Various rock types were collected in hydrothermal sites and the surrounding region, including basalt, peridotite, and gabbro [25]. A total of 8 hydrothermal black smoker clusters were observed in the study area, which are all developed within 300 m of the termination of a detachment fault. Among them, 3 clusters (A1, A2, and A3) were active and emitting hydrothermal fluid, and 5 clusters (E1, E2, E3, E4, and E5) were extinct (Figure 1b,c) [26].

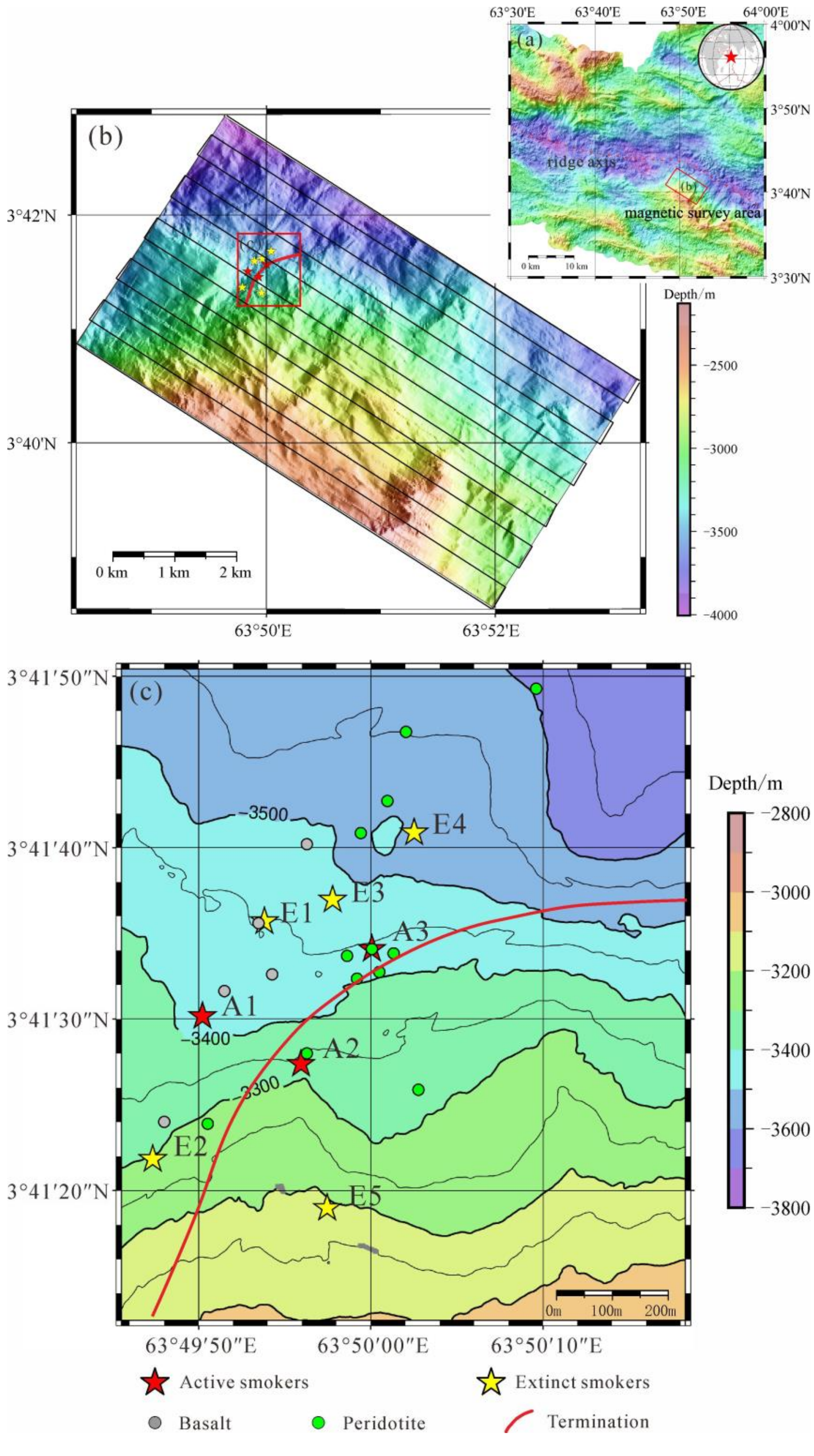

Figure 1. Bathymetry map of the survey area on the Carlsberg Ridge and location of the Tianxiu Vent Field (TVF) (bathymetry data from China DY24 cruise; resolution 50 m.). (**a**) Regional location of the Carlsberg Ridge and the survey area; (**b**) bathymetry map showing the survey area and the near-bottom magnetic detection lines (black solid lines); (**c**) bathymetry map of TVF showing the locations of sulfide chimneys (stars), sampling stations (dots), and the detachment fault (solid red line) inferred from topography and geological sampling.

3. Data Collection and Processing

High-resolution vector magnetic field data were collected using the three-axis fluxgate magnetometer system installed at the tail of the AUV. The vehicle posture (heading, roll, and pitch) data of the AUV were collected by the inertial navigation system installed in the middle of the AUV. A total of 12 near-bottom magnetic survey profiles were designed in the study area. Each line was 8000 m long, and the spacing between the profiles was 400 m. The AUV operated at the nominal altitude of 100 m above the seafloor, which varies between 50 to 150 m due to the complex terrain.

The near-bottom magnetic data processing primarily involves corrections for the vehicle-induced field and the normal magnetic field. The former mainly involved eliminating the influence of the AUV magnetic field from the magnetic data. In this study, the calibration operation and correction methods of Honsho et al. [27] and Bloomer et al. [28] were applied for the carrier magnetic disturbance correction. The latter was performed on the total magnetic field by using the international geomagnetic reference field (IGRF). Considering the short duration of the near-bottom magnetic measurements and the small effect of diurnal geomagnetic variation on the near-bottom magnetism relative to the thousands of nT amplitude variations in the near-bottom magnetism, no such correction was conducted for the data.

To eliminate the high-frequency short-wavelength noise of the magnetic anomaly caused by inconsistent terrain clearance, the data were filtered using a Butterworth low-pass filter to eliminate the high mutational sites. Next, the magnetic anomaly was converted to the new observation height of a terrain constant altitude difference (100 m) after filtering using the COMPU-DRAPETM technique [29], realizing height correction. Subsequently, low-pass filtering of the magnetic anomaly was performed to smooth the data. Figure 2 shows the processing result of the representative profile L7. After all of the 12 profiles were processed, the resulting magnetic anomaly data were interpolated to form grid data with 90 m spacing.

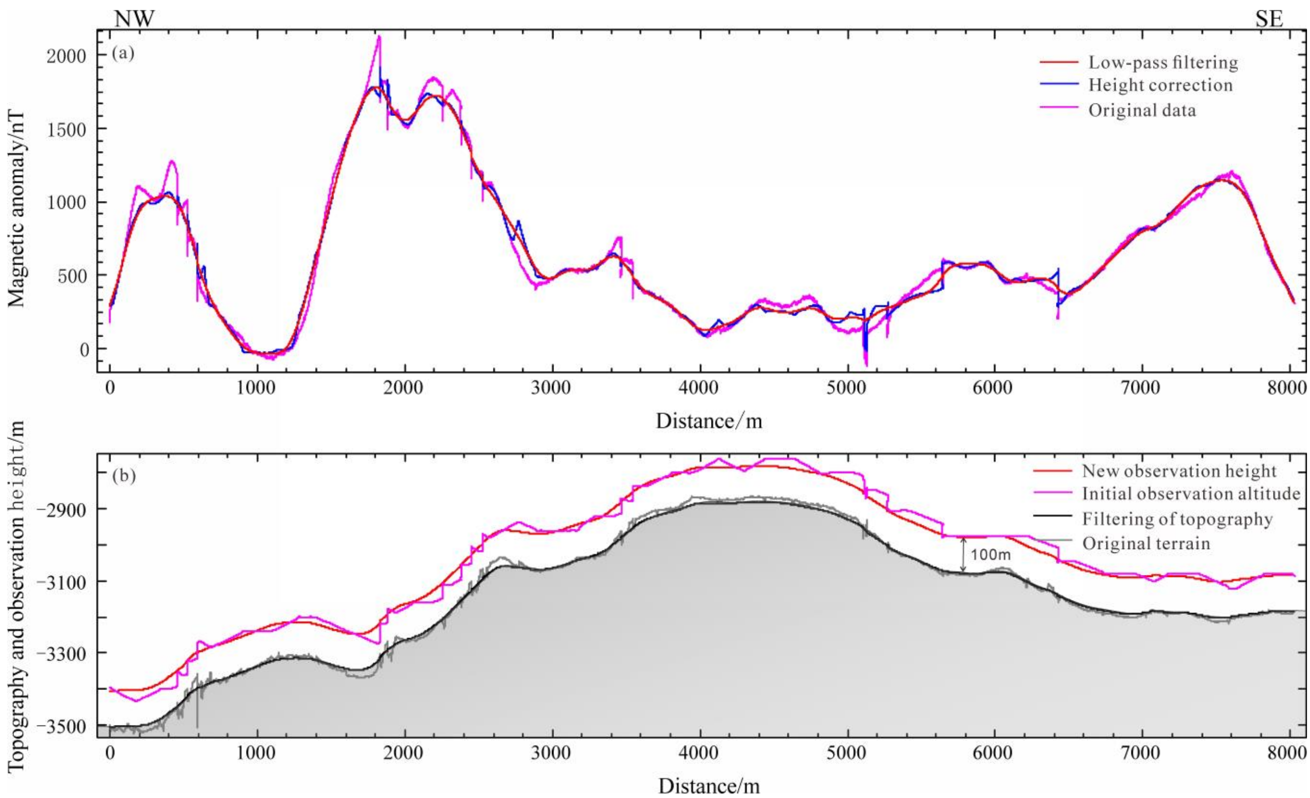

Figure 2. Example of a typical measurement line (L7) after magnetic anomaly height correction and low-pass filtering. (**a**) Magnetic anomaly data and (**b**) bathymetric profile and observation height.

The geological structures and hydrothermal fluid channels beneath the hydrothermal vents are of great research interest. Consequently, two survey lines (L7 and L8), which run through Tianxiu active hydrothermal smoker clusters, were chosen for the 2.5D forward modeling of the magnetic anomaly profile (the profile position is the red straight line in Figure 3a). To accomplish this, a base geological model was first constructed to calculate the magnetic responses based on a standard oceanic crust model as well as a mid-ocean ridge detachment fault model. Then, the semi-automatic trial-and-error method was used to adjust the distribution of seafloor magnetic structures, which were limited by lithology and rock sampling. The method's accuracy was tested by comparing the error between the model magnetic response and the observed data to ensure the best fit [21,22,30]. The forward modeling in this paper was carried out using the GM-SYS module of Geosoft's Oasis montaj software. GM-SYS Profile is a program that calculates the gravitational and magnetic response from a geological profile model. It provides an easy-to-use interface for interactively creating and debugging models to create rapid geological models. The following hypotheses were also made before forward modeling: (a) The geomagnetic inclination of the model field was considered to be consistent with that of the Earth's magnetic field. In other words, the induced and residual magnetizations were considered comprehensively as induced magnetization; therefore, the set magnetic susceptibility values differ from the actual measured magnetic susceptibility of rock, and were only used for the interpretation of the correspondence between the geological body and the magnetic susceptibility. (b) The magnetic susceptibility within lithologic blocks is uniform. According to IGRF, the magnetic anomaly calculation parameters were set as follows: total geomagnetic field = 38312 nT, declination = $-2.7865°$, inclination = $-7.5445°$, and azimuth angle of the survey line = $122.6°$.

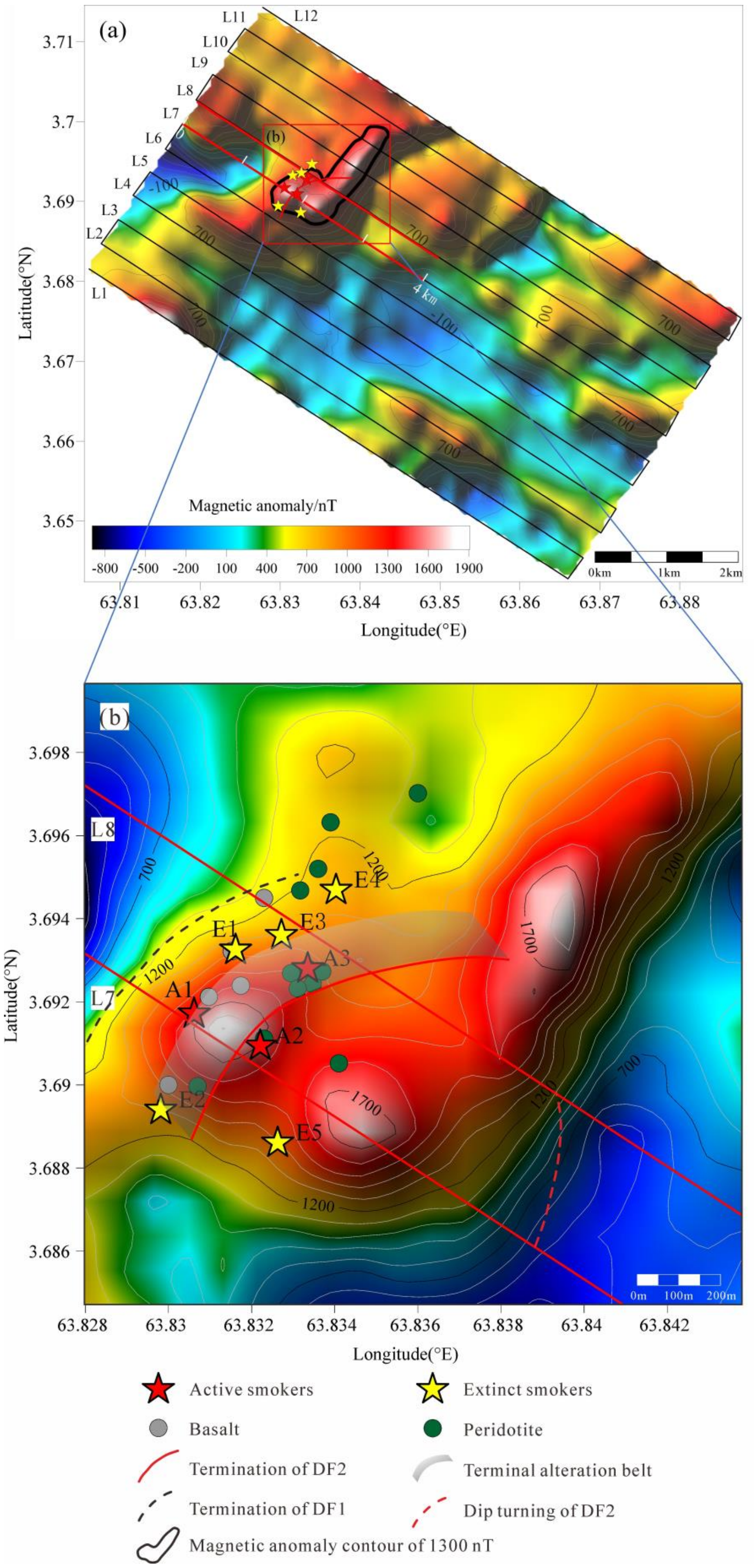

Figure 3. Distribution of magnetic anomalies in the TVF and its surrounding regions. (**a**) The survey area and (**b**) the TVF area. The red straight lines show the segments of profiles L7 and L8 used for forward modeling.

4. Results and Discussion

4.1. Magnetic Anomaly Features and Sources

The magnetic anomalies in the survey area vary from −810 to 2010 nT (Figure 3a). In the central and southern parts of the survey area, they are relatively low and vary from −200 to 200 nT. In the western and northern parts, they are characterized by positive magnetic anomalies, varying from 1000 to 2000 nT. The area with magnetic anomalies exceeding 1300 nT is approximately 0.9 km^2. The surface of the footwall of the detachment fault evidenced by the presence of serpentinized peridotites generally presents a strong positive magnetic anomaly. There are three peaks located in the south, southwest, and north of the area reaching 1800 nT. Conversely, the intensity of the magnetic anomaly of the hanging wall of the detachment fault evidenced by the presence of basalts is significantly reduced (Figure 4b). The positive magnetic anomaly intensity of the hanging wall of the detachment fault decreased significantly. The line of the E4-E3-E1-A1-E2 hydrothermal vents is close to the 1300 nT contour. The intensity of the magnetic anomaly gradually decreases to the northwest from this contour until it crosses a NE–SW magnetic anomaly gradient boundary at the 200 m position on the northwest side of A1 and quickly reduces to less than 1000 nT.

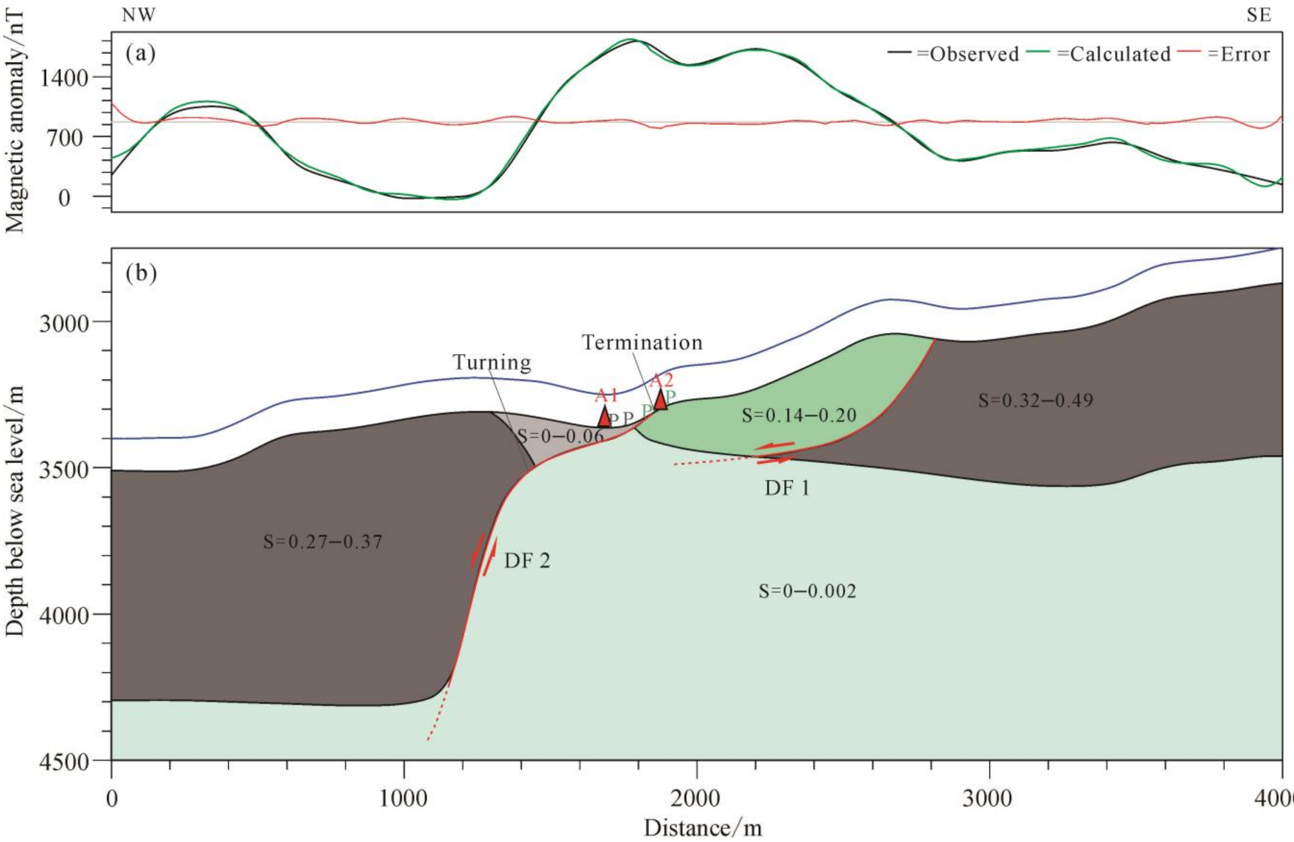

Figure 4. Forward model of the magnetic anomaly of the L7 profile in the TVF (the profile position is the red straight line in Figure 3a). (**a**) Observed and calculated magnetic anomaly and (**b**) the subsurface magnetic structure and detachment fault morphology. In Figure (**b**), the blue line denotes the observation surface, which was 100 m away from the bottom and the red triangle represents the projection positions of black smokers A1 and A2 on the profile. The gray "P" and the green "P" refer to the projection positions of basalt and peridotite sampling stations on the profile. The red solid line corresponds to the modeled detachment fault distribution, while the red dotted line represents the deduced part of the detachment fault. S denotes the magnetic susceptibility.

The observation of thin sections of rock samples under a microscope shows that the peridotite samples have been subject to severe serpentinization, with abundant magnetite grains present in serpentine veins [25]. Therefore, it is considered that the high magnetic anomalies observed in the footwall of the detachment fault in the TVF are caused by the serpentinization of peridotite. The peridotite originally in the upper mantle is uplifted to the seafloor during the detaching process, and interacts with seawater to create strongly magnetized magnetite accumulated in the mineralized zones below the hydrothermal sites. Meanwhile, the high temperature environment of hydrothermal eruption will promote the increase in magnetite proportion in serpentinization products [31]. This is consistent with the positive magnetic anomaly of other ultramafic-associated hydrothermal systems [9,31,32]. However, in the northern part of the area near E4, serpentinized peridotite was sampled, but the positive magnetic anomaly was not very strong. Therefore, this region could belong to the hanging wall of the detachment fault, with the presence of peridotite talus originating from the footwall. This is consistent with the topography of the region, which is apron-like. According to the distribution of the magnetic anomaly and rock sampling information, it is determined that the termination of the detachment fault is a 120 m wide alteration belt extending from the southwest to the northeast in the area (Figure 3b). Among the three locations with extremely high magnetic anomalies, hydrothermal black smokers have been observed in the vicinity of both the southwestern and southern ones, while the northeastern region has not been explored yet. We infer that an ultramafic-hosted hydrothermal deposit is likely to exist in this region. This is to be confirmed by future investigations.

4.2. Subsurface Magnetic Structure and Detachment Fault Morphology

Figure 4 shows the forward model of the magnetic anomaly for profile L7. The dark gray areas (magnetic susceptibility: 0.27–0.37, international system of units, denoted as S below) are dominated by mafic rocks, while the light green region (S: 0–0.002) is dominated by peridotite. These two zones are dissected by detachment faults. The green region (S: 0.14–0.20) at the footwall of the detachment fault may represent the oceanic core complex (OCC) dominated by serpentinized mantle peridotite and gabbro, with a thickness of ~300 m and a width of ~1000 m. The wedge-shaped light gray region at the hanging wall near the termination of the detachment fault is ~350 m wide and ~100 m thick, with a magnetic susceptibility reduced to 0–0.06. Based on geological sampling, this region is dominated by hydrothermally altered basalt, which explains the decrease in magnetism. Figure 5 illustrates the forward model of the magnetic anomaly for profile L8, which is similar to the model for L7. The dark-gray region (S: 0.18–0.30) corresponds to the layer dominated by mafic rocks, while the light-green region (S: 0–0.002) denotes the layer dominated by peridotite. This may represent the green area of the OCC dominated by serpentinized mantle peridotite and gabbro (S: 0.14–0.20), with an average thickness of ~280 m and a width of ~800 m. The light-gray area dominated by altered basalt is ~500 m wide and ~150 m deep, with a magnetic susceptibility reduced to 0–0.07. In both models, the peridotite alteration zone on the superficial layer extends about 100 m to the northwest beyond the termination, which supports the previous inference that the termination is an alteration zone.

Based on the obtained results of forward modeling of a magnetic anomaly in the model, it can be argued that the detachment fault (DF2) slipped from 2800 m to 1850 m along the NW in the horizontal direction on the L7 profile, and the detaching distance is about 950 m. The superficial dip angle of the fault is ~15°, changing suddenly to 70° at a depth of 300 m. The fault has extended towards deep areas for more than 1000 m. On the L8 profile, the detachment fault (DF2) has slipped from 2660 m to 2050 m along the NW in the horizontal direction, with a detaching distance of about 600 m. The superficial dip angle is ~30°, changing to 70° at a depth of 220 m. The fault extended towards deep areas for more than 800 m. The now-deactivated fault (DF1) may be located on the magnetization boundary between the OCC and the basaltic host-rock in the footwall of the two profiles. This fault is hidden below the detachment surface of DF2, and the dip angle is very small (~8°). The location where the dip of DF2 turns in the L7 and L8 profile models is located 350 m northwest of the DF2′s termination in the planar projection, and the termination of DF1 is about 700 m southeast of the DF2′s termination in the planar projection (marked as a black dashed line and red dashed line in Figure 3b, respectively). They both roughly coincide with the magnetic anomaly gradient boundary, indicating that the magnetic distribution of the hydrothermal sites can reflect the subsurface morphology of the detachment fault. The range of high magnetic anomalies on the L7 profile is wider than that on the L8 profile, with two adjacent maximum points of magnetic anomalies. Additionally, the detaching range of the detachment fault is wider, the extension depth is deeper, and the alteration range of the footwall peridotite and basalt is wider, indicating that the fracture structure below L7 is more developed than that below L8.

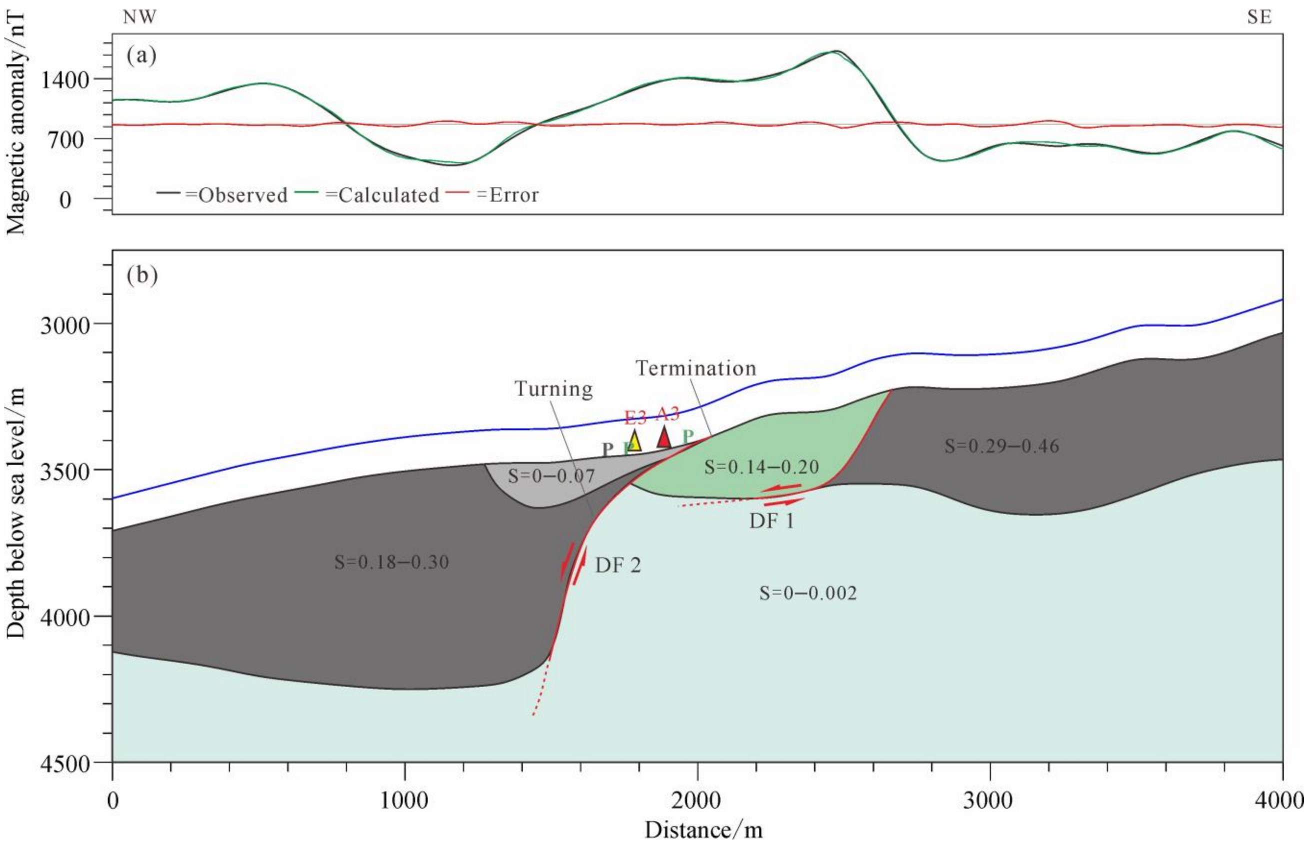

Figure 5. Forward model of the magnetic anomaly of the L8 profile in the TVF (the profile position is the red straight line in Figure 3a). (**a**) Observed and calculated magnetic anomaly and (**b**) the subsurface magnetic structure and detachment fault morphology. In Figure (**b**), the blue line denotes the observation surface, which was 100 m away from the bottom. The red and yellow triangles represent the projection positions of black smokers A3 and E3 on the profile. The gray "P" and the green "P" denote the projection positions of basalt and peridotite sampling stations on the profile, respectively. The red solid line corresponds to the modeled detachment fault distribution, while the red dotted line represents the deduced part of the detachment fault. S denotes the magnetic susceptibility.

In comparison to general detachment faults with a low angle and large displacement [33], the detachment fault (DF2) in TVF has a short detachment surface and a steep dip angle, with a morphology similar to that of the detachment fault in Rainbow hydrothermal areas [34]. According to Mccaig et al. [35], different types of hydrothermal systems are related to the evolution stages of the detachment fault: (1) In the early detaching stage, ultra-mafic rocks are not exposed to the seabed, which might produce hydrothermal vents similar to the TAG type in the Atlantic. Most of these vents are located in basalt at the hanging wall of the fault, and fluids hardly penetrate the footwall of the fault. (2) With continuous detaching, the deep gabbro and peridotite are exposed, inducing the development of Rainbow-like high-temperature hydrothermal vents at the ultrabasic basement of the footwall. (3) With further detaching of the footwall and increasing off-axis distances, the heat source might gradually cool, causing high-temperature hydrothermal vents to shift to ultra-mafic low-temperature hydrothermal vents similar to those in the Lost City. Thus, the detachment fault of TVF is relatively young and still in the second stage, which is the developing stage, conforming to the rolling hinge model of detachment faults [36]. In other words, normal faults with high dip angles begin to detach at deep and shallow regions into low angles through the rotation of the footwall. The development of the detachment fault and secondary fissure structure (e.g., DF1 and DF2) provides channels for hydrothermal circulation, facilitating the upward and lateral transport of hydrothermal fluids to bring the surrounding rocks into a full reaction with hydrothermal fluids. As a result, focused hydrothermal vents have formed in the terminal fracture zone of the detachment fault, which manifest as active and extinct black smokers. This area has high permeability, and the hydrothermal fluid is fully mixed with cold seawater. This suggests that the evolution of hydrothermal vents and sulfide deposits is greatly controlled by the evolution of the detachment fault over the long term.

5. Conclusions

Based on the first near-bottom magnetic surveys of the ultramafic-associated Tianxiu Vent Field on the slow-spreading Carlsberg Ridge, positive magnetic anomalies are detected at the hydrothermal sites. Through the processing and analysis of magnetic anomaly data, combining with the rock samples, two survey lines are selected for 2.5D magnetic anomaly profile forward modeling, leading to the following conclusions:

(1) The area where active hydrothermal vent clusters are located exhibited stronger magnetization due to the presence of magnetite produced by peridotite serpentinization. Based on the correspondence between magnetic anomalies and rock samples, it is presumed that the termination of the detachment fault is a terminal alteration belt approximately 120 m wide.

(2) The major detachment fault (DF2) running through the hydrothermal sites has a relatively short detachment surface, extending about 900 m from southeast to northwest. Its shallow dip angle is less than 30° and increases to approximately 70° at a depth of ~300 m. The fault has extended downward for more than 1000 m. There might be an inactive detachment fault with a low angle (about 8°) beneath the DF2′s detachment surface. The turning point of the dip angle in the deep areas of the DF2 corresponds to the gradient boundary of the near-bottom magnetic anomaly, indicating that the magnetic anomalies can reflect the deep morphology of the detachment fault.

(3) There may be undiscovered hydrothermal vents near sites with high magnetic anomalies about 600 m east of Tianxiu hydrothermal black smokers, where hydrothermal activity may have been happening. This area is recommended for further investigation.

Author Contributions: Conceptualization, Z.W. and X.H.; methodology, Z.W. and X.H.; validation, Z.W., X.H., Y.W. and H.L.; formal analysis, Z.W. and X.H.; investigation, Z.W., X.H. and Y.W.; resources, Z.W. and X.H.; data curation, Z.W. and X.H.; writing—original draft preparation, S.D.; writing—review and editing, S.D., Z.W., X.H., H.L. and J.Z.; supervision, Z.W. and X.H.; project administration, Z.W. and X.H.; funding acquisition, Z.W. and X.H. All authors have read and agreed to the published version of the manuscript.

Funding: This research was funded by the National Key Research and Development Program of China (No. 2021YFF0501304 and No. 2021YFF0501301), the China Ocean Mineral Resources R&D Association project (DY135-S2-1), the Talent Program of Zhejiang Province (Grant No. R51003) and Natural Science Youth Fundation of Zhejiang Province (No. LQ19D060006).

Institutional Review Board Statement: Not applicable.

Informed Consent Statement: Not applicable.

Data Availability Statement: Not applicable.

Acknowledgments: We would like to thank the captain, the crew, and the scientific parties onboard during the DY57th cruise in 2019. We are grateful to all the reviewers and editors for their contributions to this paper. We would like to thank Mingcai Hou of Chengdu University of Technology for his contribution to this article.

Conflicts of Interest: The authors declare no conflict of interest.

References

1. Corliss, J.B.; Dymond, J.; Gordon, L.I.; Edmond, J.M.; Von Herzen, R.; Ballard, R.D.; Green, K.; Williams, D.; Bainbridge, A.; Crane, K. Submarine Thermal Springs on the Galapagos Rift. *Science* **1979**, *203*, 1073–1083. [CrossRef]
2. Hannington, M.D.; de Ronde, C. Sea-Floor Tectonics and Submarine Hydrothermal Systems. In *One Hundredth Anniversary Volume*; GeoScienceWorld: McLean, VA, USA, 2005; Volume 1905, pp. 111–141.
3. Tao, C.; Li, H.; Jin, X.; Zhou, J.; Wu, T.; He, Y.; Deng, X.; Gu, C.; Zhang, G.; Liu, W. Seafloor hydrothermal activity and polymetallic sulfide exploration on the southwest Indian ridge. *Chin. Sci. Bull.* **2014**, *59*, 2266–2276. [CrossRef]
4. Rona, P.A.; Hannington, M.D.; Raman, C.V.; Thompson, G.; Tivey, M.K.; Humphris, S.E.; Lalou, C.; Petersen, S. Active and Relict Sea-Floor Hydrothermal Mineralization at the Tag Hydrothermal Field, Mid-Atlantic Ridge. *Econ. Geol.* **1993**, *88*, 1989–2017. [CrossRef]
5. Kent, D.V.; Gee, J. Magnetic alteration of zero-age oceanic basalt. *Geology* **1996**, *24*, 703–706. [CrossRef]
6. De Ronde, C.E.J.; Hannington, M.D.; Stoffers, P.; Wright, I.C.; Ditchburn, R.G.; Reyes, A.G.; Baker, E.T.; Massoth, G.J.; Lupton, J.E.; Walker, S.L.; et al. Evolution of a Submarine Magmatic-Hydrothermal System: Brothers Volcano, Southern Kermadec Arc, New Zealand. *Econ. Geol.* **2005**, *100*, 1097–1133. [CrossRef]
7. Szitkar, F.; Dyment, J.; Choi, Y.; Fouquet, Y. What causes low magnetization at basalt-hosted hydrothermal sites? Insights from inactive site Krasnov (MAR 16°38′ N). *Geochem. Geophys. Geosyst.* **2014**, *15*, 1441–1451. [CrossRef]
8. Dyment, J.; Tamaki, K.; Horen, H.; Fouquet, Y.; Nakase, K.; Yamamoto, M.; Ravilly, M.; Kitazawa, M. A Positive Magnetic Anomaly at Rainbow Hydrothermal Site in Ultramafic Environment. In *AGU Fall Meeting Abstracts*; American Geophysical Union: Washington, DC, USA, 2005; Volume 2005, p. OS21C-08.
9. Tivey, M.A.; Dyment, J. The Magnetic Signature of Hydrothermal Systems in Slow Spreading Environments. In *Diversity Of Hydrothermal Systems On Slow Spreading Ocean Ridges*; Rona, P.A., Devey, C.W., Dyment, J., Murton, B.J., Eds.; American Geophysical Union: Washington, DC, USA, 2010; pp. 43–66.
10. Charlou, J.L.; Donval, J.P.; Konn, C.; OndréAs, H.; Fouquet, Y.; Jean-Baptiste, P.; Fourré, E. High Production and Fluxes of H_2 and CH_4 and Evidence of Abiotic Hydrocarbon Synthesis by Serpentinization in Ultramafic-Hosted Hydrothermal Systems on the Mid-Atlantic Ridge. *Geophys. Union Geophys. Monogr. Ser.* **2010**, *188*, 265–296.
11. Kowalczyk, P. Geophysical Exploration for Submarine Massive Sulfide Deposits. In Proceedings of the OCEANS'11 MTS/IEEE KONA, Waikoloa, HI, USA, 19–22 September 2011.
12. Wu, T.; Tao, C.; Liu, C.; Li, H.; Wu, Z.; Wang, S.; Chen, Q. Geomagnetic Models and Edge Recognition of Hydrothermal Sulfide Deposits at Mid-ocean Ridges. *Mar. Georesour. Geotechnol.* **2015**, *34*, 630–637. [CrossRef]
13. Tivey, M.A. High-resolution magnetic surveys over the Middle Valley mounds, northern Juan de Fuca Ridge. *Proc. Ocean. Drill. Program Sci. Results* **1994**, *139*, 29–35.
14. Johnson, H.P.; Karsten, J.L.; Vine, F.J.; Smith, G.C.; Schonharting, G. A low-level magnetic survey over a massive sulfide ore body in the Troodos ophiolite complex, Cyprus. *Mar. Technol. Soc. J.* **1982**, *16*, 76–80.
15. Tao, C.; Wu, T.; Liu, C.; Li, H.; Zhang, J. Fault inference and boundary recognition based on near-bottom magnetic data in the Longqi hydrothermal field. *Mar. Geophys. Res.* **2017**, *38*, 17–25. [CrossRef]
16. Galley, C.G.; Jamieson, J.W.; Lelièvre, P.G.; Farquharson, C.G.; Parianos, J.M. Magnetic imaging of subseafloor hydrothermal fluid circulation pathways. *Sci. Adv.* **2020**, *6*, c6844. [CrossRef] [PubMed]
17. Tivey, M.A.; Rona, P.A.; Schouten, H. Reduced crustal magnetization beneath the active sulfide mound, TAG hydrothermal field, Mid-Atlantic Ridge at 26° N. *Earth Planet. Sci. Lett.* **1993**, *115*, 101–115. [CrossRef]
18. Szitkar, F.; Dyment, J.; Fouquet, Y.; Honsho, C.; Horen, H. The magnetic signature of ultramafic-hosted hydrothermal sites. *Geology* **2014**, *42*, 715–718. [CrossRef]
19. Caratori Tontini, F.; de Ronde, C.E.J.; Yoerger, D.; Kinsey, J.; Tivey, M. 3-D focused inversion of near-seafloor magnetic data with application to the Brothers volcano hydrothermal system, Southern Pacific Ocean, New Zealand. *J. Geophys. Res. Solid Earth* **2012**, *117*, B10102. [CrossRef]
20. Han, X.; Wang, Y.; Li, X. First Ultramafic-Hosted Hydrothermal Sulfide Deposit Discovered on the Carlsberg Ridge, Northwest Indian Ocean. In Proceedings of the Third InterRidge Theoretical Insitute, Hangzhou, China, 25–27 September 2015.
21. Rasmussen, R.; Pedersen, L.B. End corrections in potential field modeling. *Geophys. Prospect.* **1979**, *27*, 749–760. [CrossRef]
22. Talwani, M.; Heirtzler, J.R. Computation of Magnetic Anomalies Caused by Two Dimensional Structures of Arbitary Shape. In *Computers in the Mineral Industries*; Stanford University Press: Redwood City, CA, USA, 1964; pp. 464–480.
23. Kamesh Raju, K.A.; Chaubey, A.K.; Amarnath, D.; Mudholkar, A. Morphotectonics of the Carlsberg Ridge between 62°20′ and 66°20′ E, northwest Indian Ocean. *Mar. Geol.* **2008**, *252*, 120–128. [CrossRef]

24. Han, X.; Wu, Z.; Qiu, B. Morphotectonic Characteristics of the Northern Part of the Carlsberg Ridge near the Owen Fracture Zone and the Occurrence of Oceanic Core Complex Formation. In Proceedings of the AGU Fall Meeting Abstracts, Washington, DC, USA, 25–27 December 2012; American Geophysical Union: Washington, DC, USA, 2012; Volume 2012, p. OS13B-1722.
25. Chen, Y.; Han, X.; Wang, Y.; Lu, J. Precipitation of Calcite Veins in Serpentinized Harzburgite at Tianxiu Hydrothermal Field on Carlsberg Ridge (3.67° N),Northwest Indian Ocean: Implications for Fluid Circulation. *J. Earth Sci.* **2020**, *31*, 91–101. [CrossRef]
26. Zhou, P.; Han, X.; Wang, Y.; Wu, X.; Zong, T.; Yu, X.; Liu, J.; Li, H.; Qiu, Z. Hydrothermal Alteration of Basalts in the Ultramafic-Associated Tianxiu Vent Field, Carlsberg Ridge. *Mar. Geol.* 2023, *under review*. [CrossRef]
27. Honsho, C.; Ura, T.; Kim, K. Deep-sea magnetic vector anomalies over the Hakurei hydrothermal field and the Bayonnaise knoll caldera, Izu-Ogasawara arc, Japan. *J. Geophys. Res. Solid Earth* **2013**, *118*, 5147–5164. [CrossRef]
28. Bloomer, S.; Kowalczyk, P.; Williams, J.; Wass, T.; Enmoto, K. Compensation of Magnetic data for Autonomous Underwater Vehicle Mapping Surveys. In Proceedings of the 2014 IEEE/OES Autonomous Underwater Vehicles (AUV), Oxford, MS, USA, 6–9 October 2014.
29. Paterson Norman, R.; Reford Stephen, W.; Kwan Karl, C.H. Continuation of Magnetic Data between Arbitrary Surfaces: Advances and Applications. In *SEG Technical Program Expanded Abstracts 1990*; Society of Exploration Geophysicists: Houston, TX, USA, 1990; Volume 60, pp. 666–669.
30. Lim, A.; Brönner, M.; Johansen, S.E.; Dumais, M.-A. Hydrothermal Activity at the Ultraslow-Spreading Mohns Ridge: New Insights From Near-Seafloor Magnetics. *Geochem. Geophys. Geosyst.* **2019**, *20*, 5691–5709. [CrossRef]
31. Szitkar, F.; Tivey, M.A.; Kelley, D.S.; Karson, J.A.; Früh-Green, G.L.; Denny, A.R. Magnetic exploration of a low-temperature ultramafic-hosted hydrothermal site (Lost City, 30° N, MAR). *Earth Planet. Sci. Lett.* **2017**, *461*, 40–45. [CrossRef]
32. Fujii, M.; Okino, K.; Sato, T.; Sato, H.; Nakamura, K. Origin of magnetic highs at ultramafic hosted hydrothermal systems: Insights from the Yokoniwa site of Central Indian Ridge. *Earth Planet. Sci. Lett.* **2016**, *441*, 26–37. [CrossRef]
33. Escartín, J.; Canales, J.P. Detachments in Oceanic Lithosphere: Deformation, Magmatism, Fluid Flow, and Ecosystems. *Eos Trans. Am. Geophys. Union* **2011**, *92*, 31. [CrossRef]
34. Gràcia, E.; Charlou, J.L.; Radford-Knoery, J.; Parson, L.M. Non-transform offsets along the Mid-Atlantic Ridge south of the Azores (38° N–34° N): Ultramafic exposures and hosting of hydrothermal vents. *Earth Planet. Sci. Lett.* **2000**, *177*, 89–103. [CrossRef]
35. Mccaig, A.M.; Cliff, R.A.; Escartin, J.; Fallick, A.E.; Macleod, C.J. Oceanic detachment faults focus very large volumes of black smoker fluids. *Geology* **2007**, *35*, 935–938. [CrossRef]
36. Buck, W.R. Flexural rotation of normal faults. *Tectonics* **1988**, *5*, 959–973. [CrossRef]